ACS APPLIED MATERIALS & INTERFACES

www.acsami.org

Research Article

Redox-Channeling Polydopamine-Ferrocene (PDA-Fc) Coating To Confer Context-Dependent and Photothermal Antimicrobial Activities

Jialin Song,[‖] Huan Liu,[‖] Miao Lei, Haoqi Tan, Zhanyi Chen, Artem Antoshin, Gregory F. Payne, Xue Qu,* and Changsheng Liu*

Cite This: *ACS Appl. Mater. Interfaces* 2020, 12, 8915−8928

Read Online

ACCESS | Metrics & More | Article Recommendations | Supporting Information

ABSTRACT: Microbial disinfection associated with medical device surfaces has been an increasing need, and surface modification strategies such as antibacterial coatings have gained great interest. Here, we report the development of polydopamine-ferrocene (PDA-Fc)-functionalized TiO_2 nanorods (Ti-Nd-PDA-Fc) as a context-dependent antibacterial system on implant to combat bacterial infection and hinder biofilm formation. In this work, two synergistic antimicrobial mechanisms of the PDA-Fc coating are proposed. First, the PDA-Fc coating is redox-active and can be locally activated to release antibacterial reactive oxygen species (ROS), especially ·OH in response to the acidic microenvironment induced by bacteria colonization and host immune responses. The results demonstrate that redox-based antimicrobial activity of Ti-Nd-PDA-Fc offers antibacterial efficacy of over 95 and 92% against methicillin-resistant *Staphylococcus aureus* (MRSA) and *Escherichia coli (E. coli)*, respectively. Second, the photothermal effect of PDA can enhance the antibacterial capability upon near-infrared (NIR) irradiation, with over 99% killing efficacy against MRSA and *E. coli*, and even suppress the formation of biofilm through both localized hyperthermia and enhanced ·OH generation. Additionally, Ti-Nd-PDA-Fc is biocompatible when tested with model pre-osteoblast MC-3T3 E1 cells and promotes cell adhesion and spreading presumably due to its nanotopographical features. The MRSA-infected wound model also indicates that Ti-Nd-PDA-Fc with NIR irradiation can effectively eliminate bacterial infection and suppress host inflammatory responses. We believe that this study demonstrates a simple means to create biocompatible redox-active coatings that confer context-dependent antibacterial activities to implant surfaces.

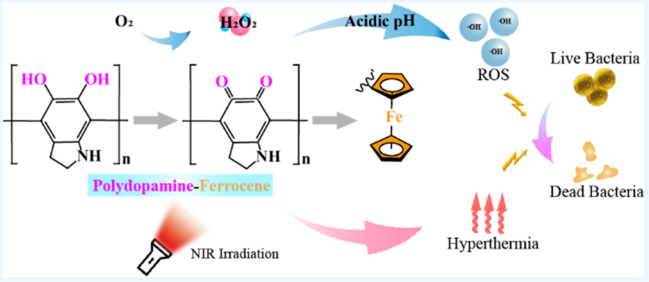

KEYWORDS: *implant, antibacterial, redox, polydopamine, hydroxy radical, photothermal, chemodynamic therapy*

1. INTRODUCTION

Bacterial contamination presents a serious ongoing problem in areas ranging from industrial operations (e.g., food manufacturing) to human health.[1] In particular, bacterial infections at the site of implanted medical devices may result in chronic diseases and even death of the patient.[2] Indeed, about 45% of all nosocomial infections are associated with medical devices.[3,4] A common strategy to prevent contamination is to apply antimicrobial coatings to substrate surfaces,[5] and therefore, the development of antimicrobial coatings is attracting significant attention.[6−8]

Several types of antimicrobial coatings have been developed so far,[9] which can be divided into two broad categories: anti-adhesion coating and bactericidal coating. Generally, anti-adhesion coatings are based on antifouling polymers, such as poly(ethylene glycol) (PEG) and its derivatives[10,11] and zwitterion-containing polymers.[12] These coatings are capable of repelling bacterial adhesion and attachment through nonspecific interactions. Bactericidal coatings are designed to provide direct bacterial killing mechanisms and are usually preloaded with antibiotics,[13,14] antibacterial peptides,[15] enzymes,[16] quaternary ammonium compounds (QACs),[17−19] or metal nanoparticles.[20] Although numerous antimicrobial coating strategies have been proposed and demonstrate general effectiveness against both Gram-positive and Gram-negative bacteria, present antimicrobial coatings, however, still have some drawbacks. For instance, anti-adhesion coatings sometimes lack effective and stable antimicrobial activities, while bactericidal coatings may result in premature depletion of their active ingredient and induce adverse effects (e.g., tissue injury) or promote the emergence of drug resistance. In fact, the rise

Received: December 10, 2019
Accepted: January 23, 2020
Published: January 23, 2020

https://dx.doi.org/10.1021/acsami.9b22339
ACS Appl. Mater. Interfaces 2020, 12, 8915−8928

Scheme 1. Fabrication Process of Ti-Nd-PDA-Fc, Putative Structural Unit of PDA-Fc, Redox-Based Antimicrobial Activity, and Photothermally Enhanced Antimicrobial Activity[a]

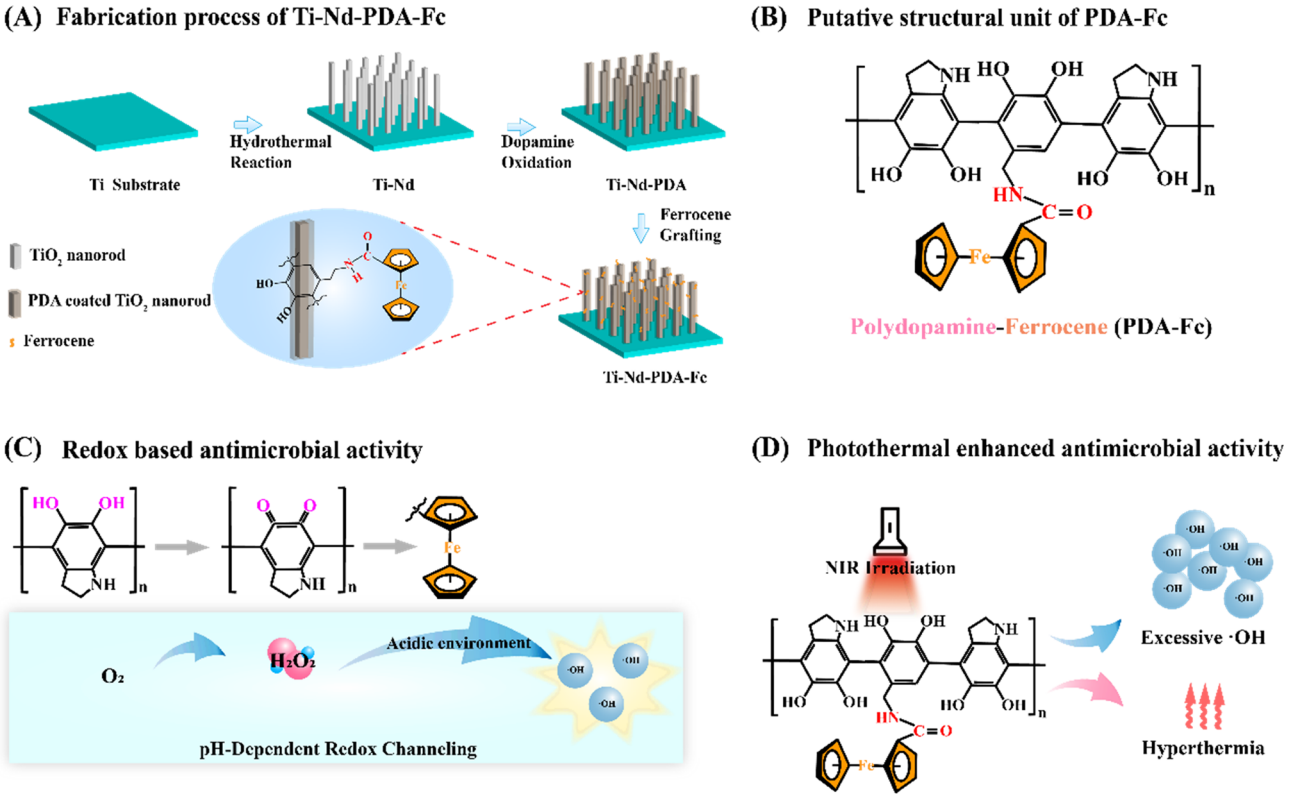

[a](A) Synthesis process of Ti-Nd-PDA-Fc on the Ti substrate. TiO_2 nanorods are grown on the Ti substrate by the hydrothermal reaction. PDA is derived from self-polymerization of dopamine in Tris−HCl buffer with pH 8.5. Also, ferrocene is covalently grafted on PDA coating through EDC-NHS chemistry. (B) Putative structural unit of PDA-Fc coating. (C) Redox-based antimicrobial activity by inducing ·OH generation. (D) Photothermally enhanced antimicrobial activity through both excessive ·OH generation and hyperthermia.

of multidrug-resistant bacteria is becoming a major clinical concern.[21]

A major biological approach to fight bacterial infections is the generation of reactive oxygen species [ROS; e.g., superoxide (O^{2-}), hydrogen peroxide (H_2O_2), hydroxy radical (·OH), and nitric oxide radical (NO·)],[22] and ROS-based antibacterial therapies are attracting great attention.[23] Owing to the unique oxidative killing mechanism, ROS-based antimicrobial approaches have been reported to have higher efficacy with lower side effects compared with conventional treatments[24] and to be active against a wide spectrum of pathogens, including multidrug-resistant isolates.[25] Notably, ROS-releasing antimicrobial therapies can be designed to be activated locally by diverse stimuli, such as pH values,[26,27] temperature,[28] and light,[29,30] which makes them a good candidate for the "context-dependent" designs.

Here, we report a biomimetic redox-active antimicrobial coating capable of the in situ generation of reactive oxygen species (ROS), which has similarities to emerging chemodynamic anticancer therapies that employ nanomaterials to promote ROS generation.[31] Titanium implant is one of the common medical devices[32] and used as the model substrate in this work. Specifically, Scheme 1A illustrates that we prepared a nanostructured surface by generating TiO_2 nanorods (Ti-Nd) using a hydrothermal method because such nanostructured surfaces have been reported to suppress bacterial adhesion.[33] We then coated the Ti-Nd nanostructured surface by the self-polymerization of dopamine to make polydopamine (PDA)-coated Ti-Nd (Ti-Nd-PDA). Because PDA coatings are simple to generate and relatively easy to functionalize, they have been applied for a wide range of applications,[34−37] including the coating of implant surfaces to confer antimicrobial activities.[38,39] Finally, Ti-Nd-PDA is functionalized by the covalent grafting of the iron (Fe)-containing organometallic compound ferrocene (Fc) to prepare PDA-Fc-coated Ti-Nd (Ti-Nd-PDA-Fc). The putative chemical structure of PDA-Fc coating on Ti-Nd-PDA-Fc is illustrated in Scheme 1B.

In terms of functionality, our previous study demonstrates that PDA nanoparticles are redox-active,[40] and Scheme 1C hypothesizes that the catecholic moieties of PDA coating will be redox-active and capable of donating electrons to O_2 to generate H_2O_2.[41,42] We propose that this H_2O_2 will be an intermediate that is "channeled" into the highly reactive ·OH radical via a Fenton-like reaction by the Fc moiety.[43] Importantly, the conversion of H_2O_2 to ·OH is promoted by acidic conditions that characterize the pH context associated with bacterial infections (Note that the pH value in the severe infection sites can be as low as 5.0−5.5, as previously reported).[44,45] Although the hypoxia in the infection site is recently reported[46] and our ROS-generating approach requires O_2, we should note that the absolute O_2 concentration in the infection site has only 20% decrease,[47] where the immune system can also utilize the O_2-dependent antimicrobial mechanism to combat bacterial infection. On the other hand, we foresee that, due to the extreme toxicity, a small amount of

https://dx.doi.org/10.1021/acsami.9b22339
ACS Appl. Mater. Interfaces 2020, 12, 8915−8928

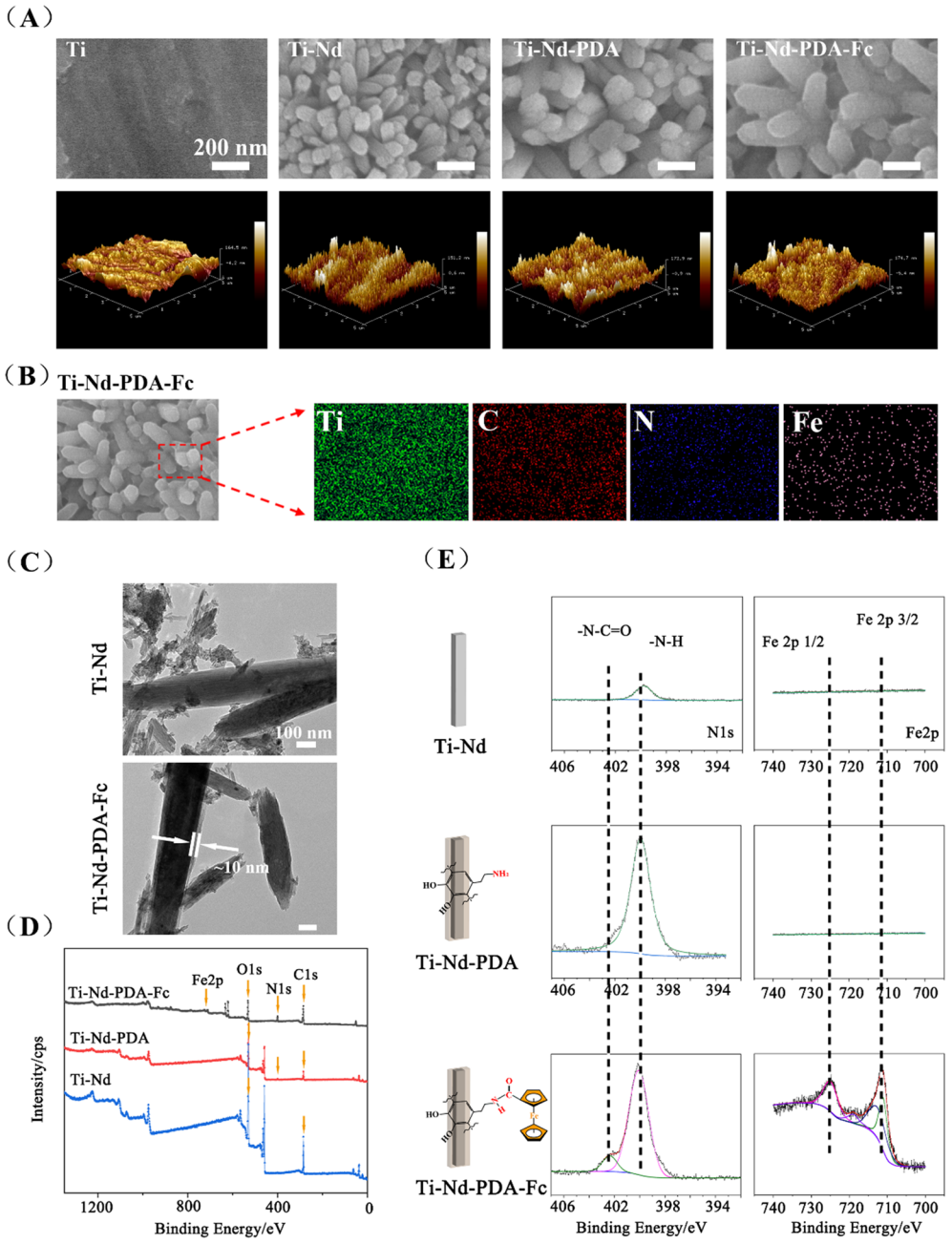

Figure 1. (A) FE-SEM and AFM images of different substrates. Scale bars are 200 nm. (B) EDS mapping (Ti, C, N, and Fe) images of Ti-Nd-PDA-Fc. (C) TEM images of Ti-Nd and Ti-Nd-PDA-Fc. Scale bars are 100 nm. (D) XPS survey spectra of Ti-Nd, Ti-Nd-PDA, and Ti-Nd-PDA-Fc surfaces. (E) High-resolution XPS spectra of N 1s and Fe 2p on Ti-Nd, Ti-Nd-PDA, and Ti-Nd-PDA-Fc surfaces.

OH free radicals derived from O_2 can also provide valid oxidative stress to bacteria.

In addition, Scheme 1D suggests that the PDA component of this coating may also confer photothermal properties that improve antimicrobial activities upon near-infrared (NIR) irradiation due to photothermal heating and potentially enhanced ROS generation.[48] Moreover, we provide chemical, cell, and animal studies to support the proposed functions of Ti-Nd-PDA-Fc.

We believe that this Ti-Nd-PDA-Fc antimicrobial design offers three important advantages. First, the PDA-Fc coating spatially localizes ROS generation to the implant surface. Second, it limits ·OH-generating activities to the acidic contexts that characterize bacterial infections. Third, it enables the application of a second synergistic antimicrobial mechanism based on exogenously triggered photothermal hyperthermia.

2. RESULTS AND DISCUSSION

2.1. Fabrication and Characterization of Ti-Nd-PDA-Fc. Titanium nanorods were first prepared on the polished titanium substrates by a facile one-step hydrothermal method (150 °C; 2 h in acidic solution), as previously reported.[49] The as-synthesized titanium substrates with TiO_2 nanorods (Ti-Nd) were then gently incubated in 50 mL of dopamine hydrochloride solution (2 mg/mL; pH 8.5) overnight to prepare Ti-Nd-PDA substrates. After an ascorbate reduction

https://dx.doi.org/10.1021/acsami.9b22339
ACS Appl. Mater. Interfaces 2020, 12, 8915−8928

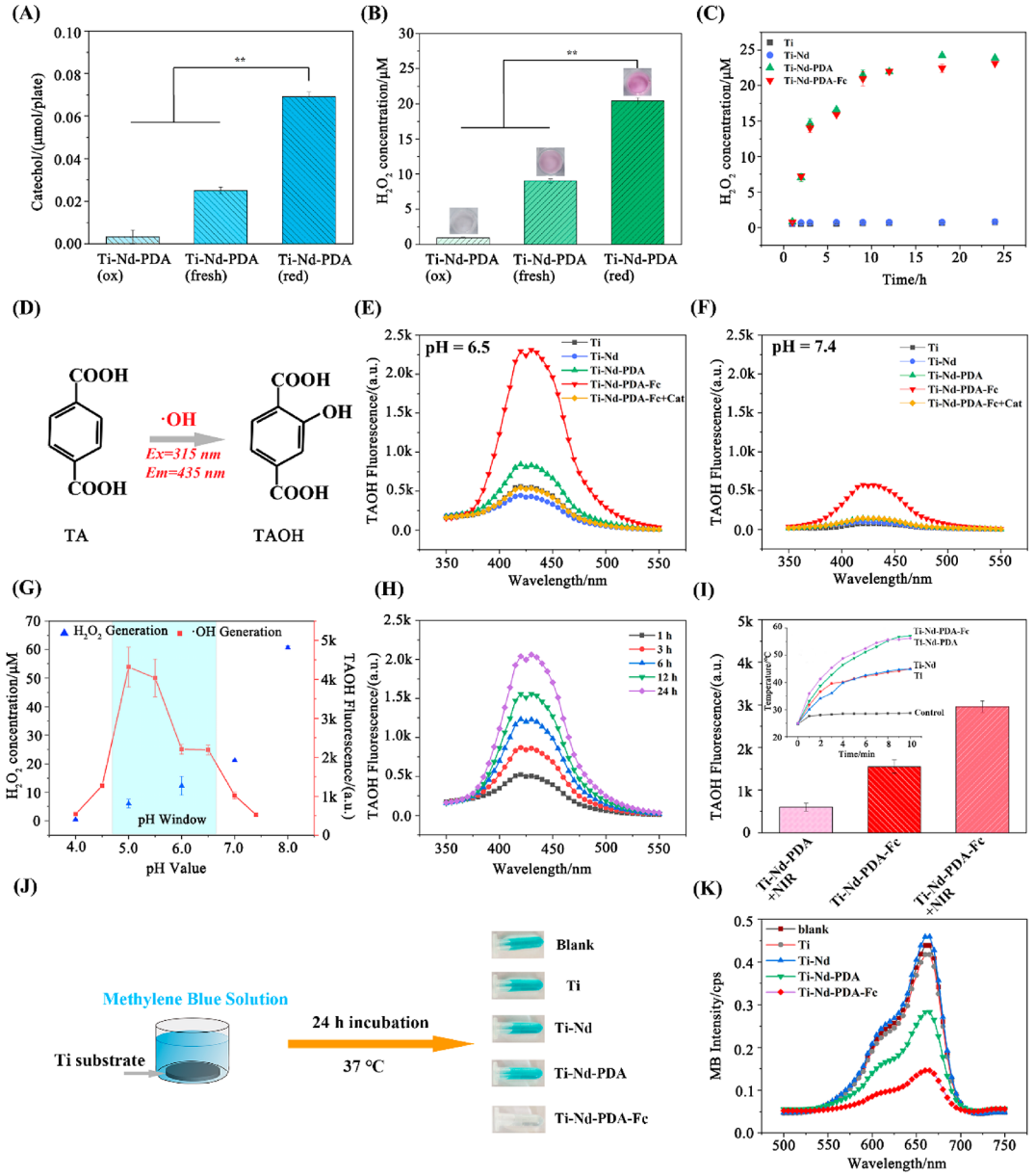

Figure 2. (A) Catechol content and (B) H_2O_2 generation of Ti-Nd-PDA at different redox states. (The color changes of Amplex Red indicator dye are inserted.) (C) H_2O_2 generation of Ti-Nd-PDA-Fc in 1 mL of PBS buffer (10 mM) for a determined time at pH 7.4. (D) Reaction between ·OH and terephthalic acid (TA). (E, F) Fluorescence spectra of the TA solution with pH 6.5 and pH 7.4, respectively, co-incubated with Ti, Ti-Nd, Ti-Nd-PDA, Ti-Nd-PDA-Fc, and Ti-Nd-PDA-Fc + Cat for the 24 h reaction. "Cat" stands for catalase and was used to quench H_2O_2. (G) Fluorescence spectra of the TA solution (50 mM) co-incubated with Ti-Nd-PDA-Fc and H_2O_2 generation of Ti-Nd-PDA for 24 h at different pH values. Blue area indicates the pH window. (H) Fluorescence spectra of the TA solution (pH 6.5, 50 mM) co-incubated with Ti-Nd-PDA-Fc for a determined time. (I) Fluorescence spectra of the TA solution (pH 6.5, 50 mM) co-incubated with Ti-Nd-PDA and Ti-Nd-PDA-Fc with or without NIR irradiation. The inset is the temperature changes of the substrates when exposed to NIR irradiation; PB buffer is used as the control group. (J) Schematic illustration of the MB degradation experiment where the Ti substrate is immersed in MB solution and photographs of degraded MB solution. (K) Degradation of MB (2 mg/mL, 2 mL) solution with adsorption peak at 665 nm in aqueous solution using different substrates for 24 h. Ascorbate-reduced Ti-Nd-PDA is used for the experiments in (C), unless otherwise mentioned.

step, ferrocene was covalently grafted on PDA coating through EDC-NHS chemistries.[50]

Some methods were used for morphological characterization. Field-emission scanning electron microscopy (FE-SEM) and atomic force microscopy (AFM) in Figure 1A revealed that titanium nanorods were successfully synthesized, and the array-like morphology was composed of an individual nanorod vertically grown on the substrate, with an approximate diameter of 100 nm. The X-ray diffraction (XRD) spectrum in Figure S1a showed a titanium dioxide crystal diffraction pattern with a rutile TiO_2 phase (JCPDS no. 21-1276).[51] Compared with the standard pattern of titanium, the relative intensities of (101) and (002) peaks were significantly enhanced, confirming the existence of a single crystal of titanium dioxide. Figure 1B shows the energy-dispersive spectroscopy (EDS) mapping of Ti-Nd-PDA-Fc for Ti, C, N, and Fe elements. These results demonstrated that all the elements were distributed uniformly, confirming the existence of PDA coating and ferrocene on the surface of Ti-Nd-PDA-Fc. Transmission electron microscopy (TEM) images in

https://dx.doi.org/10.1021/acsami.9b22339
ACS Appl. Mater. Interfaces 2020, 12, 8915−8928

Figure S1b also demonstrated that the length of Ti-Nd was approximately 1 μm. Following the self-polymerization of dopamine and the subsequent grafting of ferrocene, Ti-Nd exhibited a slight increase in diameter, while the nanorod-shaped morphology was still retained. According to the TEM images in Figure 1C, the increase in thickness was about 10 nm, which explained the undeformed morphology.

Furthermore, X-ray photoelectron spectroscopy (XPS) analysis was carried out. The apparent N peak on Ti-Nd-PDA and Fe and N peaks on Ti-Nd-PDA-Fc are observed in the XPS survey spectra in Figure 1D. It was worth noting that the C peak on Ti-Nd might ascribe to the contamination during the hydrothermal process. Also, the high-resolution XPS spectra of both N 1s and Fe 2p in Figure 1E revealed that C−N and C═N peaks were detected in the Ti-Nd-PDA-Fc substrate at binding energies of 402 and 399.5 eV, respectively,[52] indicating the presence of chemical bonds within the PDA coating. Meanwhile, the Fe 2p peaks were also characteristically observed at binding energies of 726 and 712 eV,[53] representing the Fe $2p_{3/2}$ and Fe $2p_{1/2}$ peaks, respectively, suggesting the successful grafting of ferrocene onto the PDA coating. The Fourier-transform infrared (FTIR) spectra of Ti-Nd-PDA and Ti-Nd-PDA-Fc in Figure S1c also confirm the amide linkage formed between polydopamine and ferrocene.

In addition, the contact angles in Figure S2 of Ti, Ti-Nd, Ti-Nd-PDA, and Ti-Nd-PDA-Fc were 99.75°, 53.33°, 37.50°, and 35.50°, respectively, demonstrating better hydrophilicity after surface modification.

2.2. Chemical Characterization of ROS Generation. As illustrated in Scheme 1C, one function of PDA component in the antimicrobial coating is to generate the intermediate H_2O_2. According to our previous work, H_2O_2 generation depends on the redox state of PDA. Thus, Ti-Nd-PDA substrates with different redox states were tested using the Folin−Ciocalteu reagent.[54] Specifically, we tested: as-prepared Ti-Nd-PDA substrates (designated Ti-Nd-PDA (fresh)), Ti-Nd-PDA substrates oxidized by air treatment at 60 °C for 2 days (designated Ti-Nd-PDA (ox)), and Ti-Nd-PDA substrates reduced by 100 mM ascorbate solutions for 30 min (designated Ti-Nd-PDA (red)). Figure 2A shows that the phenol content was obviously higher on Ti-Nd-PDA (red), suggesting its higher content of donatable electrons to oxygen for H_2O_2 generation.

In addition, we measured the H_2O_2 generation from Ti-Nd-PDA samples with different redox states. Specifically, H_2O_2 generation was measured by enzymatic (horse radish peroxidase, HRP) colorimetric assay with the Amplex Red indicator dye. In this assay, the dye is colorless but switches into a pink-colored product upon an HRP-catalyzed reaction with H_2O_2. Figure 2B shows that Ti-Nd-PDA (red) generated the highest concentration of H_2O_2, which is consistent with its higher level of donatable electrons. Finally, various substrates were incubated and then monitored for H_2O_2 generation over the course of 24 h. Figure 2C reveals that Ti-Nd-PDA and Ti-Nd-PDA-Fc had continuously increasing H_2O_2 levels during 24 h incubation, reaching values of about 25 μM H_2O_2. (Note that the pH of these solutions was 7.4, which precluded the Fc-catalyzed conversion of H_2O_2 into ·OH.) Even though H_2O_2 is clinically used for disinfection, H_2O_2 still has some limitations: the low efficiency and slow process. In fact, a burst release of medical concentrations of H_2O_2 (0.5−3%) usually do harm to normal tissues and hamper wound healing when treating bacterial infections. In this work, H_2O_2, being an intermediate, is continuously generated via a redox reaction in situ and further channeled into much more toxic ·OH in the infection sites, thus developing the localized and instant antibacterial treatment.

The ability of Fc moiety to convert the H_2O_2 intermediate into ·OH was tested using terephthalic acid (TA) as a fluorescence probe for ·OH tracking. As illustrated in Figure 2D, the product 2-hydroxyl terephthalic acid (TAOH) was measured by its fluorescence emission at 435 nm.[55] When 24 h incubations were performed under mildly acidic conditions (pH 6.5), the emission spectrum observed in Figure 2E for the case of Ti-Nd-PDA-Fc indicated high levels of ·OH generation. This high fluorescence intensity was not observed when Ti-Nd-PDA-Fc was incubated with the catalase enzyme that could catalyze the degradation of the H_2O_2 intermediate. When Fc was not included in the coating or the Ti was uncoated, considerably less fluorescence was observed, which was consistent with the expectation that Fc was required to catalyze ·OH-generating Fenton-like reactions. The results in Figure 2F also indicated little ·OH generation by Ti-Nd-PDA-Fc at neutral pH (pH 7.4), which was consistent with the context-dependent (i.e., low pH-dependent) generation of ·OH.

The same ·OH and H_2O_2 generation experiment was performed at varying pH values. In detail, Ti-Nd-PDA substrates were used to observe the pH-dependent generation of H_2O_2, while Ti-Nd-PDA-Fc substrates were used to observe the pH-dependent generation of ·OH. Figure 2G shows that both ·OH and H_2O_2 generations were pH-dependent, with significant ·OH generation only being observed under a mildly acidic pH window. It is understandable that the Fenton-like reaction is activated in an acidic microenvironment to produce ·OH. But it is also noteworthy that H_2O_2 generation can be prohibited at a very acidic environment, which is also reported by Lee et al.[42] Although it has not been fully understood, we hypothesize that the acidic environment may promote the protonation of the amino group, which further restrains the electrons transferred to O_2, thus resulting in the reduced generation of H_2O_2. Figure 2H reveals results from a time-dependent experiment in which the cumulative ·OH generation was observed over a 24 h period for the Ti-Nd-PDA-Fc substrate.

In addition to its H_2O_2 generation activity, the PDA component of the coating confers a second potential antimicrobial activity: the dissipation of near-infrared (NIR) radiation can lead to a significant photothermal effect. The inset in Figure 2I shows that NIR illumination results in a marked temperature rise for PDA-coated Ti substrates, while uncoated Ti substrates show a more modest temperature rise. The heating and cooling curve of Ti-Nd-PDA-Fc is also provided in Figure S3. To evaluate whether NIR illumination affects ·OH generation, we tested different substrates with or without NIR irradiation. As expected, ·OH generation after 24 h incubation was remarkably greater for the Ti-Nd-PDA-Fc substrate with NIR irradiation, compared with Ti-Nd-PDA with NIR irradiation and Ti-Nd-PDA-Fc without NIR irradiation.

A final demonstration of the generation of damaging reactive oxygen species was performed by incubating different substrates for 24 h in the presence of methylene blue (MB) and observing the degradation of MB by a loss of its characteristic color and its maximum adsorption peak at 665

https://dx.doi.org/10.1021/acsami.9b22339
ACS Appl. Mater. Interfaces 2020, 12, 8915−8928

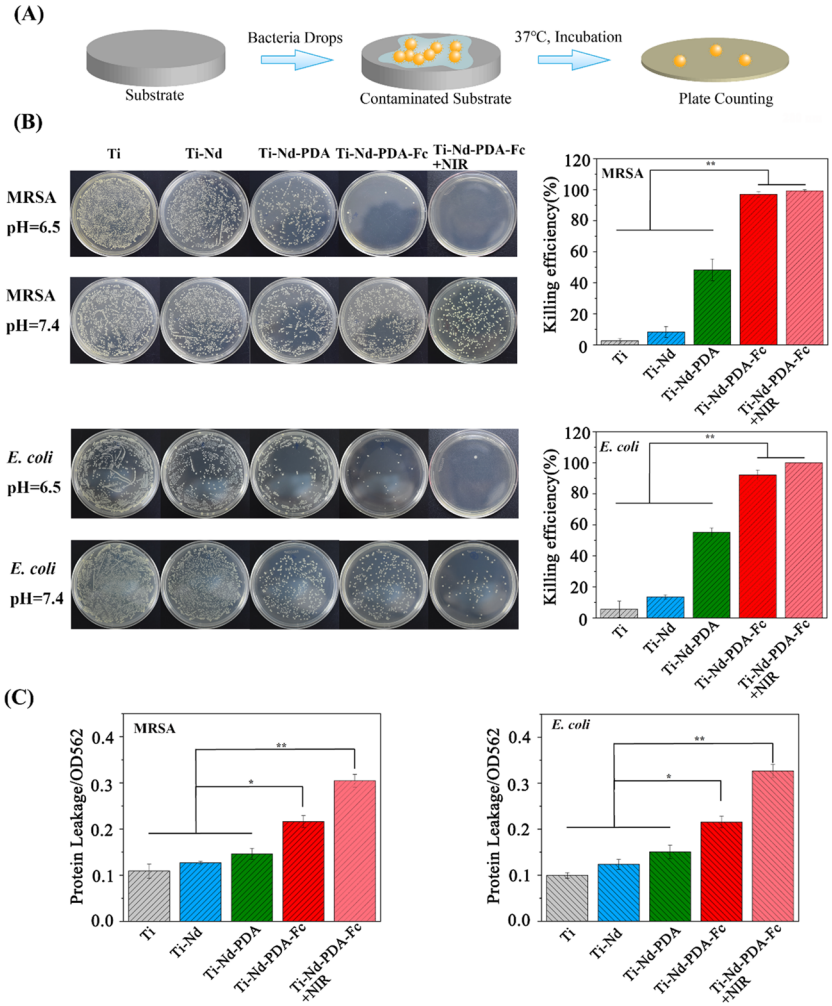

Figure 3. (A) Schematic illustration of the bacterial experiment where bacterial drops are applied on the substrate surfaces, and after determined time of incubation under 37 °C, the bacteria are collected for diluted plate counting. (B) Photographs of MRSA and *E. coli* colonies on the medium after incubation with different samples under acidic and neutral environments. Also, antibacterial activity of each substrate against MRSA and *E. coli* at pH 6.5. (C) Protein leakage of MRSA and *E. coli* on different substrate surfaces. The higher value of OD562 indicates higher protein leakage, which originates from cell membrane damage.

nm.[56] As illustrated in the photographs and UV−Vis spectra in Figure 2J,K, there was a negligible color change when MB was incubated with the Ti or Ti-Nd substrates. A partial color loss was observed when MB was incubated with the Ti-Nd-PDA substrate, which suggested that MB was partially degraded by H_2O_2 generated by PDA-containing coating. However, when MB was incubated with the Ti-Nd-PDA-Fc substrate, it displayed a nearly complete loss of color, which was consistent with the conclusion above stating that the Fc component of the coating converted the intermediate H_2O_2 into a more damaging oxidant (i.e., ·OH).

In summary, the results in Figure 2 provide chemical evidence that PDA-Fc coating can generate damaging reactive oxygen species, with the PDA component functioning to generate an H_2O_2 intermediate and the Fc component functioning to covert H_2O_2 into a more reactive ·OH radical. NIR illumination can also induce temperature increase and accelerate ·OH generation.

2.3. In Vitro Antimicrobial Activity. Initially, we envisioned two major antimicrobial mechanisms: ROS generation to kill bacteria and the NIR photothermal effect to enhanced persistent (e.g., biofilm formation) infections. Notably, the nanorod morphology had been reported with mild antibacterial adhesion.[57] Figure S4 of the Supporting Information demonstrates that nanostructuring offers moderate benefits in terms of suppressing bacterial attachment.

To examine the antimicrobial activities of our coatings, we prepared several substrates and "contaminated" them by adding bacterial drops containing 1×10^6 CFU/mL bacteria, as illustrated in Figure 3A. Gram-positive methicillin-resistant *Staphylococcus aureus* (MRSA) and Gram-negative bacteria *Escherichia coli* (*E. coli*) were used in these antimicrobial experiments. After "contamination", these substrates were incubated (37 °C) for 8 h, and then various methods were used to characterize antimicrobial activity. It is worth noting that the pH value in a severe infection site can be 5.0−5.5. But our strategy focuses more on the early antibacterial process, which is critical for successful antibacterial treatment.[58] The bacterial microenvironment at an early stage can be mildly acidic. So, we have adopted pH 6.5 in the following experiments as a pH trigger.

In one set of experiments, we performed plate counting to assess bacterial viability. The upper images in Figure 3B showed the results for MRSA. When MRSA bacteria were

https://dx.doi.org/10.1021/acsami.9b22339
ACS Appl. Mater. Interfaces 2020, 12, 8915−8928

incubated with Ti and Ti-Nd substrates, similar plate counts were observed, while incubation with the Ti-Nd-PDA substrate resulted in a somewhat lower plate count. In these three cases, the plate counts did not depend on the pH of incubation. When MRSA bacteria were incubated with the Ti-Nd-PDA-Fc substrate, nearly complete killing was observed under mildly acidic conditions, while relatively small killing was observed at neutral pH condition. The rightmost photo in Figure 3B showed results for the Ti-Nd-PDA-Fc substrate that was irradiated with NIR (808 nm for 10 min) after contamination. The results were similar to those with the nonirradiated Ti-Nd-PDA-Fc substrate. The lower photographs in Figure 3B revealed that *E. coli* responded similarly to Ti-Nd-PDA-Fc while showing a somewhat stronger response to NIR photothermal treatment, which possibly ascribed to their different cell wall structures. Quantification of these results is presented at the right part in Figure 3B.

Mechanistically, it is believed that ROS therapies and photothermal treatment kill bacteria through damage or destruction of the cell membrane, and such damage is assessed by measuring protein leakage associated with such permeability changes.[28,59] According to Figure 3C, after NIR irradiation for 10 min followed by incubation for 8 h, MRSA and *E. coli* on Ti-Nd-PDA-Fc substrates exhibit the highest protein leakage than any other groups, demonstrating that the bacterial membrane in the Ti-Nd-PDA-Fc group with NIR irradiation has experienced the most severe damage.

In a second set of experiments, the bacteria were incubated for 8 h after which they were stained for viability using the fluorescence dyes SYTO 9 (live) and PI (dead). The confocal images in Figure 4A showed a large number of green (viable) bacteria on Ti, Ti-Nd, and Ti-Nd-PDA substrates, while a large number of yellow or red (dead) bacteria were observed on the Ti-Nd-PDA-Fc substrate. In addition, it could also be seen that a large number of dead bacteria were observed when either MRSA or *E. coli* was tested with Ti-Nd-PDA-Fc substrates that were irradiated with NIR after contamination. Next, SEM images of MRSA and *E. coli* were photographed for their morphological analysis. Figure 4B demonstrates that MRSA had a smooth spherical surface on the pure Ti substrate, while a few structural perturbations were observed for these bacteria that were on Ti-Nd and Ti-Nd-PDA substrates. These results were consistent with relatively low toxicity of nanorods and PDA induced by H_2O_2 generation. Considerably greater structural distortions were apparent when MRSA bacteria were on Ti-Nd-PDA-Fc substrates or Ti-Nd-PDA-Fc substrates irradiated by NIR. For the case of *E. coli*, the SEM images in Figure 4B were similar to those for MRSA, and the structural disruptions appeared more profound when NIR was applied. The structural similarities might suggest the similar killing mechanism between MRSA and *E. coli*, which involved membrane disruption and structural deformation. In summary, the results in both Figures 3 and 4 provide valid evidence that PDA-Fc coating can confer antimicrobial activity to the Ti substrate and NIR irradiation provides synergistic antimicrobial activities.

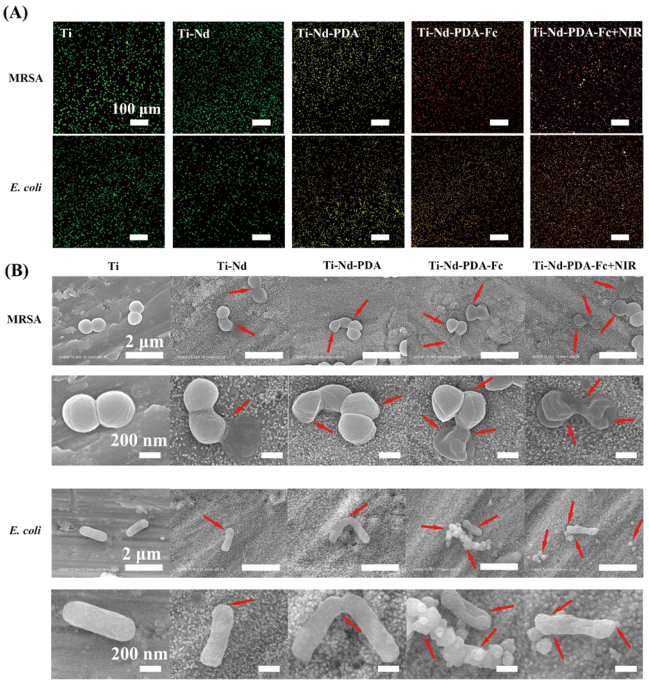

Figure 4. (A) Live and dead staining images of MRSA and *E. coli* on different substrate surfaces. Scale bars are 100 μm. (B) FE-SEM images of MRSA and *E. coli* on the substrate of Ti, Ti-Nd, Ti-Nd-PDA, Ti-Nd-PDA-Fc, and Ti-Nd-PDA-Fc + NIR. Red arrows indicate the irregular morphology of bacterial cells. Scale bars are 2 μm and 200 nm.

2.4. Suppressing Biofilm Formation with Photothermal Effects. The formation of bacterial biofilms on implant surfaces presents a significant clinical challenge as biofilms can facilitate antibiotic resistance and promote persistent infections. In this experiment, we contaminated the substrates with MRSA and incubated them in nutrient-rich medium (3% TSB medium supplemented with 1% glucose) for 24 h. Semiquantitative biofilm assay was involved to stain the biofilm with crystal violet. The results in Figure 5A showed that different levels of biofilms were formed on all substrates except the Ti-Nd-PDA-Fc substrate with NIR irradiation. Interestingly, when the H_2O_2-degrading enzyme catalase was included in the medium, there was significantly less antibiofilm activity, indicating that photothermally induced hyperthermia alone could not inhibit biofilm formation effectively. The above observation suggests that antibiofilm formation activity associated with NIR irradiation appears to result from both the generation of reactive oxygen species and a thermal effect.

Further evidence for the importance of NIR irradiation for combating extensive microbial contamination is provided by the SEM images in Figure 5B and live dead cell staining in Figure 5C. In both cases, MRSA bacteria were observed to extensively cover the substrates except for the case of NIR-irradiated Ti-Nd-PDA-Fc substrate, which showed a few viable bacteria and extensive cell debris.

2.5. Cell Viability. To be applicable clinically, the implanted materials should possess both high antimicrobial capability and good biocompatibility. The MTT measurement was applied to observe the cell viability. Specifically, the MC-3T3 E1 cells are incubated on the prepared substrates for a determined time at pH 7.4 for cell viability assay. Initial studies with pre-osteoblast MC-3T3 E1 cells in Figure 6A indicated that all the substrates were biocompatible. However, the cells' attachment behaved differently on different surfaces in Figure 6B. MC-3T3 E1 cells on the Ti substrate had a flat morphology and scatter unevenly on the surface. Zooming in on the edge of the cells, a round boundary can be observed, while conversely, the MC-3T3 E1 cells on Ti-Nd, Ti-Nd-PDA, and Ti-Nd-PDA-Fc substrates were more stereoscopic and

https://dx.doi.org/10.1021/acsami.9b22339
ACS Appl. Mater. Interfaces 2020, 12, 8915−8928

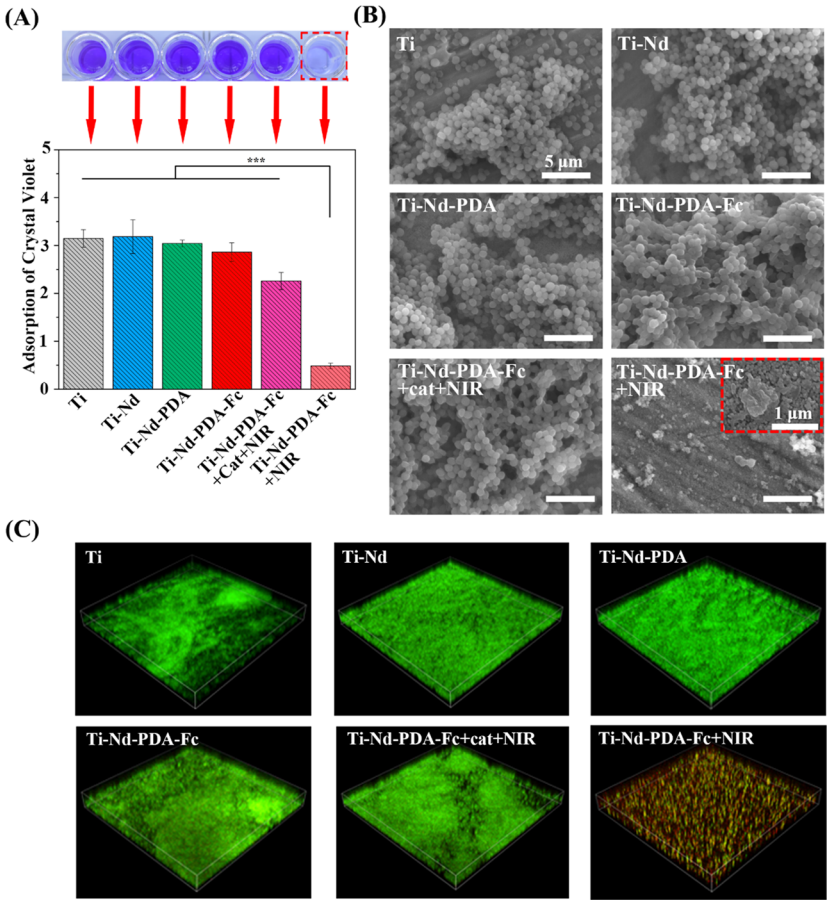

Figure 5. (A) Photographs of crystal violet-stained MRSA biofilms and their adsorptions at 590 nm (OD590). (B) SEM images of the MRSA biofilm on different substrates. Scale bars are 5 μm. The scale bar in the red block is 1 μm. (C) 3D fluorescence images of the MRSA biofilm on different substrates: Ti, Ti-Nd, Ti-Nd-PDA, Ti-Nd-PDA-Fc, Ti-Nd-PDA-Fc + cat with NIR, and Ti-Nd-PDA-Fc with NIR.

homogeneously dispersed, indicating good cell attachment to the material surface. Protein adsorption of each substrate was investigated in Figure 6C, and the results implied that the nanostructured substrates had better protein adsorption compared with the untreated substrate, which was probably a reason for the better cell adhesion and attachment of MC-3T3 E1 cells on Ti-Nd, Ti-Nd-PDA, and Ti-Nd-PDA-Fc substrates.

2.6. In Vivo Antimicrobial Activity. To evaluate in vivo antimicrobial activity, we used an MRSA-infected rat model in which MRSA-contaminated substrates were implanted subcutaneously. The rats were randomly separated into six groups of three rats per group, and as illustrated in Scheme 2, each rat had two wounds with a single contaminated substrate implanted. After 3 days, the wounds were reopened, and the infection site was photographed. The white arrows in Figure 7A indicated visible suppurations and edemas for most of the wounds, indicating wound infection. The wounds with the implanted Ti-Nd-PDA-Fc substrate that was exposed to NIR (Figure S5) did not appear to have any edema or purulence, indicating less severe (or no) inflammation.

Each of the implanted substrates was carefully recovered, and the attached bacteria were collected and quantified by dilution plate counting. Figure 7B,C shows that the H_2O_2-generating Ti-Nd-PDA substrate offered some antimicrobial activity. When the Ti-Nd-PDA substrate was exposed to NIR to confer photothermal effects, the antimicrobial activity was enhanced (compared to Ti-Nd-PGA without NIR). Similarly, when Fc was incorporated into the coating to enable the conversion of H_2O_2 to ·OH, the antimicrobial activity was also enhanced (Ti-Nd-PDA-Fc vs Ti-Nd-PDA). When the implanted Ti-Nd-PDA-Fc substrate was treated with NIR, the MRSA antimicrobial activity was further enhanced as suggested by the synergistic effect of increasing temperature and ·OH generation before. Histological evaluation of the wounds was also carried out by hematoxylin and eosin-stained sections (H&E staining). In Figure 7D, it was obvious that a large number of inflammatory cells, such as neutrophils, existed in the control groups, implying that the possible infection and immune response occurred. Instead, a significant decrease of inflammatory cells could also be observed in the Ti-Nd-PDA-Fc + NIR group. These results verified the strong antibacterial capability of Ti-Nd-PDA-Fc with NIR irradiation in vivo.

3. CONCLUSIONS

In summary, we report polydopamine and ferrocene (PDA-Fc)-functionalized TiO_2 nanorods (Ti-Nd-PDA-Fc) as an antimicrobial system that offers context-dependent ·OH generation and photothermal heating in response to NIR illumination. We started with the simple "universal" polydopamine (PDA) coating system and enlisted PDA's redox properties and photothermal effect for generation of a H_2O_2 intermediate and localized hyperthermia. Covalent incorporation of ferrocene (Fc) moieties into the coating enables the H_2O_2 intermediate to be "channeled" into a more reactive ·OH radical. Importantly, ·OH generation is maximal under the slightly acidic conditions that are typically the observed context

https://dx.doi.org/10.1021/acsami.9b22339
ACS Appl. Mater. Interfaces 2020, 12, 8915−8928

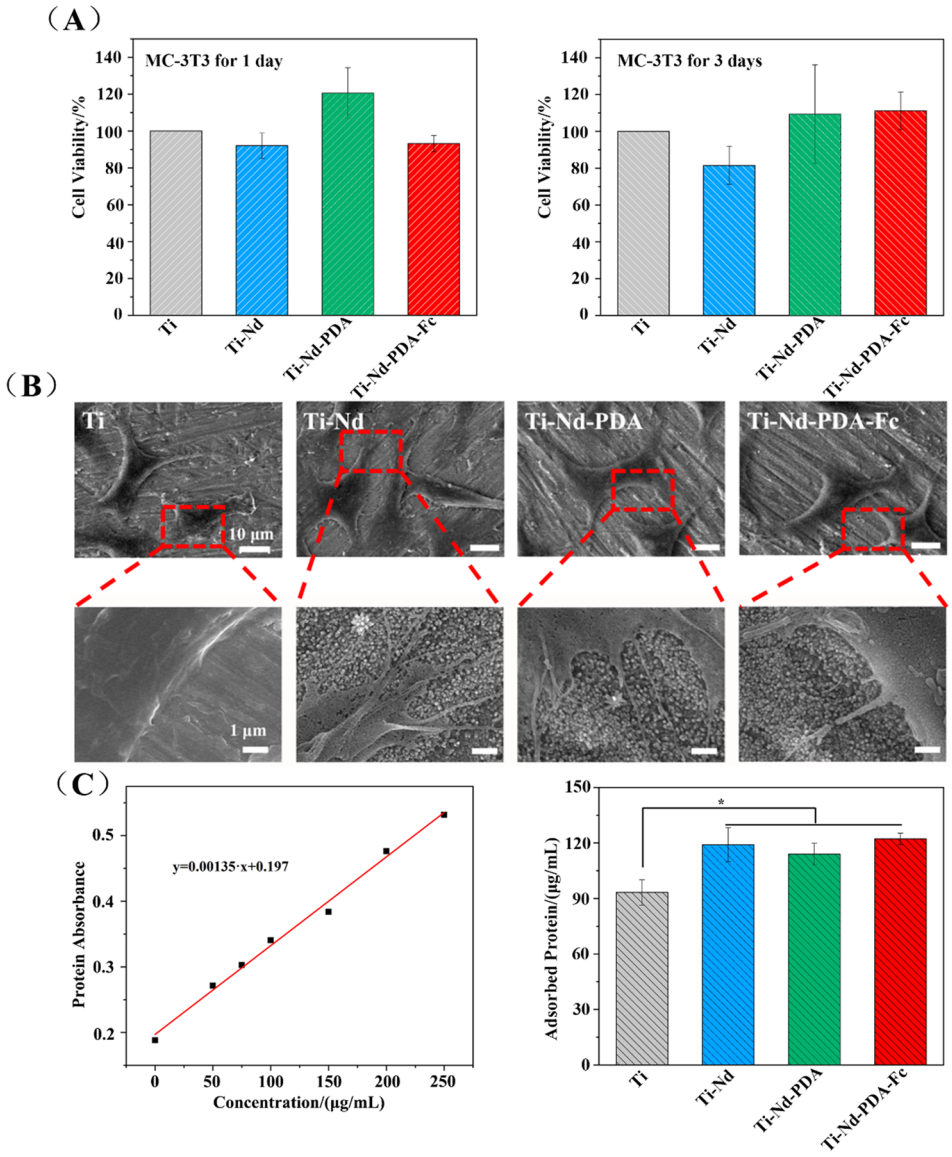

Figure 6. (A) MC-3T3 E1 cell viability on various substrates for 1 and 3 days. (B) FE-SEM images of MC-3T3 E1 cells on various substrates. Scale bars are 10 and 1 μm. (C) Standard protein adsorption curve of different protein concentrations and protein adsorption on various substrates for 24 h.

Scheme 2. Schematic Illustration of the Animal Experiment and Corresponding Antibacterial Activities at the Wound Sites

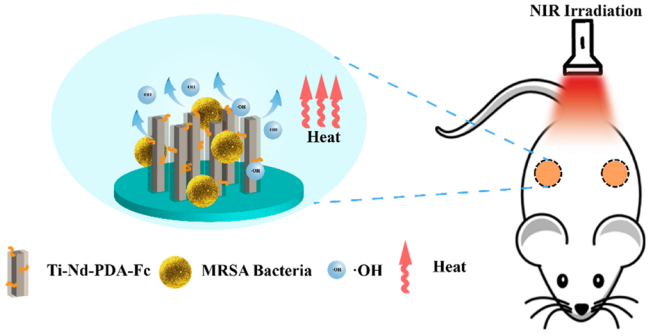

at infection sites. We demonstrate that both ·OH generation and NIR photothermal effect can contribute antimicrobial activities in vitro and in vivo. We envision that these coatings, coupling native antimicrobial mechanisms (e.g., the localized endogenous generation of ROS) with externally controllable interventions (e.g., NIR irradiation), can offer versatile means to combat bacterial infections for a range of medical applications, such as artificial vessels and antibacterial dressings.

4. MATERIALS AND METHODS

4.1. Materials. Titanium plates were purchased from Taizhou Huihuang Xincailiao Co., Ltd. Titanium butoxide (AR, ≥98.5%) was purchased from General Reagents Co., Ltd. Dopamine hydrochloride, ascorbate (reagent grade, 99%), and catalase (2000−5000 units/mg protein) were all purchased from Sigma-Aldrich. Ferrocenecarboxylic acid (reagent grade, 98%), *N*-(3-dimethylaminoproyl)-*N*′-ethylcarbodiimide hydrochloride (reagent grade, 98%), and *N*-hydroxysulfosuccinimide sodium salt (reagent grade, 98%) were obtained from Aladdin Co., Ltd. Live/Dead BacLight Bacterial Viability Kit was purchased from Invitrogen. 3-(4,5-Dimethylthiazol-2-yl)-2,5-diphenyltetrazolium bromide (MTT) was purchased from Beyotime

https://dx.doi.org/10.1021/acsami.9b22339
ACS Appl. Mater. Interfaces 2020, 12, 8915−8928

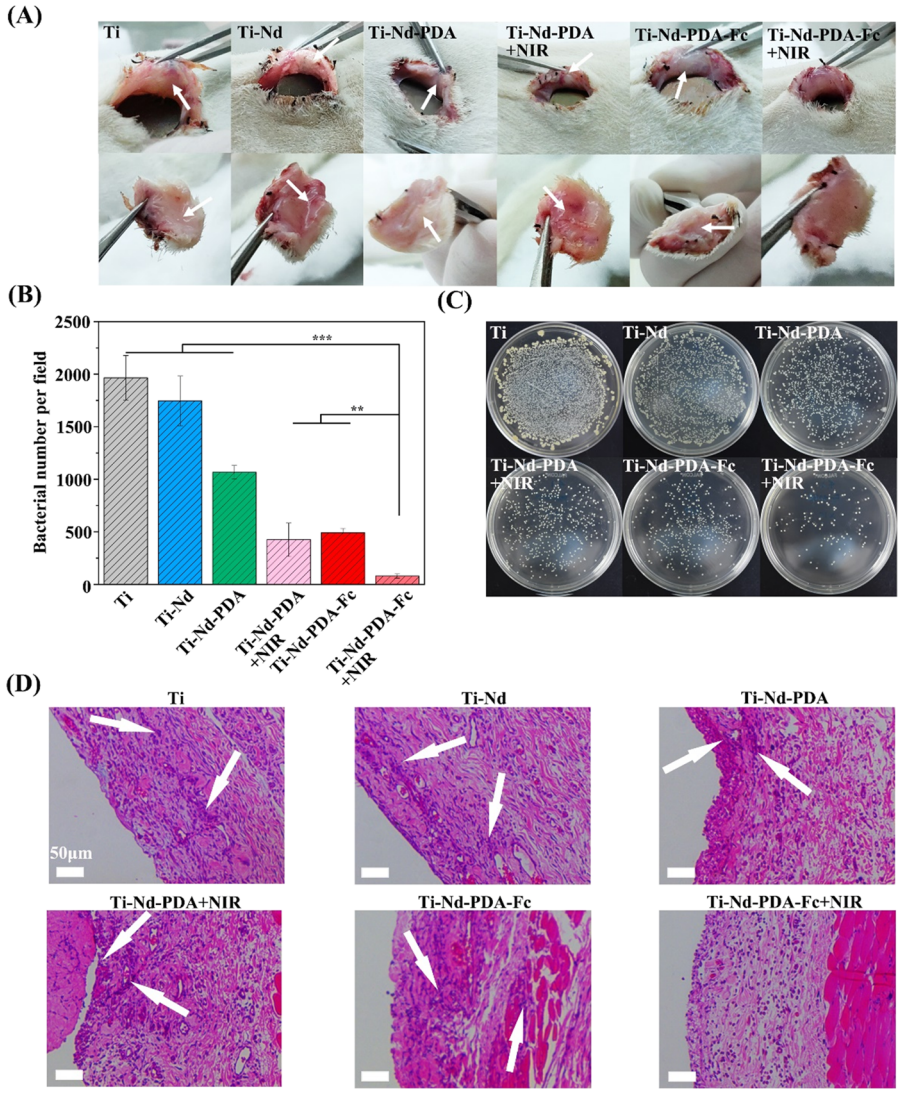

Figure 7. (A) Photographs of reopened incisions after 3 days of implantation. The substrates were preseeded with MRSA (10^7 CFU/mL, 10 μL) and then embedded into the wound site. White arrows indicate the naked eye-visible suppurations and edemas. (B) Quantification of the surviving bacteria on the plates: Ti, Ti-Nd, Ti-Nd-PDA, Ti-Nd-PDA with NIR, Ti-Nd-PDA-Fc, and Ti-Nd-PDA-Fc with NIR. (C) Remaining bacterial plate counting after being exposed to Ti, Ti-Nd, Ti-Nd-PDA, Ti-Nd-PDA with NIR, Ti-Nd-PDA-Fc, and Ti-Nd-PDA-Fc with NIR. (D) Photomicrographs for the histological analysis of wound sites by H&E staining. The white arrows indicate the aggregation of neutrophils accompanied with the possible inflammations. Scale bars are 50 μm.

Biotech Co., Ltd. All cell culture-related reagents were purchased from Gibco. The chemicals were used without further purification.

4.2. Synthesis of Ti-Nd-PDA-Fc. To synthesize titanium nanorod arrays, 10 mL of deionized water was mixed with 9 mL of concentrated hydrochloric acid (36.5−38% by weight) to reach a total volume of 19 mL in a Teflon-lined stainless-steel autoclave. The mixture was stirred at ambient conditions for 5 min before the addition of 0.5 mL of titanium butoxide. After stirring for another 5 min, four pieces of titanium plates were fixed on a Teflon substrate and placed vertically on the bottom of the container. The hydrothermal synthesis was conducted at 150 °C for 2 h in an electric oven. After the synthesis, the autoclave was cooled to room temperature under flowing water, which took about 15 min. The titanium plates were taken out for extensive rinsing with deionized water and allowed to dry in ambient air.

The synthesized titanium plates (Ti-Nd) were then gently agitated in 50 mL of dopamine hydrochloride solution (2 mg/mL) with pH 8.5 overnight to prepare Ti-Nd-PDA plates. After the coating of PDA, the substrates were rinsed and immersed in 100 mM ascorbate solution for 30 min to endow PDA a better reduced state (PDA in Ti-Nd-PDA-Fc was all in the reduced state, unless otherwise mentioned). Ferrocene was dissolved in MES solution (pH 6.0) and stirred with EDC and NHS reagents for 3 h under 500 rpm before it was grafted on Ti-Nd-PDA. Next, Ti-Nd-PDA plates were co-incubated in the ferrocene-containing MES solution for another 2 h to graft ferrocene. Finally, Ti-Nd-PDA-Fc plates were washed three times with deionized water and subsequently stored in the refrigerator to prevent its slow oxidization in the air.

4.3. Characterization. Images of size and morphology of the samples were obtained by a field-emission electron microscope (S-4800 Hitachi), atomic force microscope (Veeco/DI), and JEM-2100 (JEOL) high-resolution transmission electron microscope. XRD measurement was carried out on a D/max2550VB (Bruker) using Cu Kα radiation. Chemical analysis of the products was performed on an X-ray photoelectron spectrometer (ESCALAB 250Xi) and UV−Vis spectrophotometer (SpectraMax M2, USA). The FTIR spectra were recorded by an FTIR spectrometer (Thermo Nicolet 6700) equipped with the DTGS detector. The water contact angle was measured by a sessile drop method on a contact-angle meter (Dataphysics, OCA20). The volume of each droplet was set as 1 μL.

4.4. Detection of PDA Redox States, H_2O_2, and Hydroxyl Radical (·OH) Generation. To characterize the redox state of Ti-

https://dx.doi.org/10.1021/acsami.9b22339
ACS Appl. Mater. Interfaces 2020, 12, 8915−8928

Nd-PDA, Folin−Ciocalteu colorimetric assay was employed for characterization of the oxidative property of Ti-Nd-PDA. Briefly, each substrate was first immersed in 1.5 mL of water solution with 0.125 mL of Folin−Ciocalteu solution for 4 min, and then Na_2CO_3 solution (0.875 mL; 20.0%, w/v) was added in the dark. After 1 h co-incubation, the total solution was collected for UV−Vis analysis with absorbance at 760 nm. Next, H_2O_2 generation of Ti-Nd-PDA with different redox states was measured by horseradish peroxidase enzyme-mediated hydrogen peroxide assay kit (Amplite Fluorimetric Hydrogen Peroxide Assay Kit, AAT Bioquest). Then, to quantify H_2O_2 generation of Ti-Nd-PDA-Fc, the substrates were incubated with 1 mL of air-saturated water for a determined time. Then, an aliquot of the solution was diluted and tested by the method mentioned above.

The generation of ·OH was evaluated by monitoring the change in fluorescence of 2-hydroxy terephthalic acid (TAOH) due to the oxidation of terephthalic acid (TA) in aqueous solution. As previously reported, ·OH can reduce TA into TAOH with the maximum fluorescence peak at 435 nm. In detail, the investigated substrates were incubated in 2 mL of TA solution (50 mM) at different pH values for different times. The mixture was gently shaken and stored at 37 °C in the dark, and then changes in the fluorescence emission peak were recorded. The generation of H_2O_2 on Ti-Nd-PDAs was also detected at different pH values. The ·OH generation under NIR irradiation was tested by the above method, and the temperature curve was recorded by a thermal sensor.

Methylene blue (MB) dye was selected to demonstrate the oxidative capability of ·OH. In general, the substrates were incubated in 2 mL of MB (2 mg/mL) dye at 37 °C for 24 h in the dark. Next, the MB dye was collected for photograph and UV−Vis adsorption analysis in the range of 500−700 nm.

4.5. Bacterial Culture and Preparation. Bacteria such as Gram-negative bacteria *E. coli* (ATCC 25922) and Gram-positive bacteria methicillin-resistant *Staphylococcus aureus* (MRSA) were acquired from Second Affiliated Hospital of Zhejiang University. Single colonies of Gram-negative and Gram-positive bacteria were grown in the corresponding media, Luria−Bertani (LB) and Tryptic Soy Broth (TSB) for Gram-negative and Gram-positive bacteria, respectively, for 8 h in a 37 °C shaker. The bacterial suspensions were subjected to centrifugation and washing with 0.9% physiological saline to completely remove the bacterial culture media. Finally, the bacterial pellets were resuspended in 0.9% physiological saline at a certain concentration for further use.

4.6. Anti-Adhesion Test and ROS-Based Antibacterial Activity Assay. For the anti-adhesion activity assay of titanium nanorods (Ti-Nd), polished titanium substrates and Ti-Nd substrates were prepared and then placed in 24-well plates. Bacteria were allowed to adhere on the surface of the substrates for 2 h in a bacterial incubator at 37 °C. After incubation, the substrates were rinsed twice with PBS to remove nonadherent bacteria and placed in a new 24-well plate. Also, 1 mL of PBS and 0.5 mL of TSB mixture were added into each well and then incubated at 37 °C for 8 h. Next, a certain concentration of bacterial suspension was obtained after vigorous stirring of the samples. One hundred microliters of the bacteria suspension of each substrate was used for the optical density test at 600 nm (OD600). For the plate counting method, the acquired bacteria suspensions were separately diluted 10,000 times with PBS. Afterward, 100 μL of the diluted bacterial suspensions were spread on the solid medium and incubated at 37 °C for 12 h. The number of bacteria colonies was finally recorded. The rest of bacteria were carefully collected for TEM observation.

Antibacterial assay was conducted through co-incubation of the substrates with bacteria suspensions. Five groups of as-prepared products were used: (1) Ti, (2) Ti-Nd, (3) Ti-Nd-PDA, (4) Ti-Nd-PDA-Fc, and (5) Ti-Nd-PDA-Fc + NIR. The volume and concentration of bacteria suspension were 300 μL and 1×10^6 CFU/mL, respectively. After 8 h incubation, the bacteria suspensions were diluted 100 times, and then the plate counting method was utilized as mentioned before. The killing efficiency of both bacteria was calculated using the determined dilution for plate counting. Antibacterial efficiency was calculated by the following formula:

$$\text{antibacterial efficiency (\%)} = (\text{number of bacterial colonies on blank control} - \text{number of bacterial colonies on substrates}) / (\text{number of bacterial colonies on blank control}) \times 100\%$$

Protein leakage assay was conducted through co-incubation of the substrates with bacteria suspensions. Five groups of as-prepared products were used: (1) Ti, (2) Ti-Nd, (3) Ti-Nd-PDA, (4) Ti-Nd-PDA-Fc, and (5) Ti-Nd-PDA-Fc + NIR. The volume and concentration of bacteria suspension were 300 μL and 1×10^7 CFU/mL, respectively. After 8 h incubation, the bacteria suspensions were collected and centrifuged at 8000 rpm for 5 min. The protein concentration in the supernatant was finally determined by a BCA protein kit (BCA assay, Beyotime).

Live/Dead BacLight Bacterial Viability kits were conducted in the dark for 15 min and then imaged by confocal laser scanning microscopy. For SEM images, bacteria of corresponding groups were collected and fixed with 2% glutaraldehyde for 2 h. The bacteria were further dehydrated using 30, 50, 70, 90, and 100% ethanol. Eventually, the air-dried bacteria were observed under field-emission electron microscopy after 40 s of sputter coating with gold.

4.7. Inhibition of Biofilm Formation. A common experimental approach to create a model biofilm in vitro is to inoculate a surface with a high concentration of bacteria and provide these bacteria with nutrient-rich conditions to promote their growth.[27] For antibiofilm formation assay, 1 mL of MRSA solution (10^6 CFU/mL, 3% TSB medium, 1% glucose) was added into the substrate well and incubated at 37 °C. After incubation for 24 h, each substrate was taken out and gently washed three times with PBS. Then, all the substrates were characterized by crystal violet staining assay. The remaining crystal violet-stained biofilms were photographed and quantified by adding 100% ethanol and measuring the OD590 value of the homogeneous suspension. To visualize the biofilms on each substrate by confocal laser scanning microscopy (CLSM), biofilms with different treatments were incubated with SYTO 9 and PI (3 μL/mL) for 15 min at 37 °C in the dark and then observed by CLSM at the same parameters. SEM images of each biofilm were also obtained through the methods mentioned before.

4.8. Cell Viability Experiments. Mouse MC-3T3 E1 cells were employed for investigation of cell experiments. In vitro cytotoxicity was measured by quantitative MTT assay. First, the modified titanium substrates were carefully placed on the bottom of each well, and then MC-3T3 E1 cells were seeded with a density of 4×10^4 cells per well. After a predetermined incubation time, the cell activity of each group was carried out by the MTT method. Protein adsorption was carried out by a protein adsorption method, as previously reported.[60] All samples were first soaked in Dulbecco's modified Eagle medium with 50% fetal bovine serum at 37 °C for 24 h. Then, each sample was rinsed with PBS and incubated in 1% sodium dodecyl sulfate (SDS) for 15 min. The protein adsorption on SDS was finally determined by a BCA protein kit (BCA assay, Beyotime). In addition, CLSM and FE-SEM images were used for observation of cellular viability and morphology.

4.9. In Vivo Rat Wound Model. To assess the antibacterial ability of Ti-Nd-PDA-Fc with NIR irradiation for wound disinfection application, we successfully built the rat wound model. Male Sprague−Dawley (SD) rats (6−8 weeks) were divided into six groups: (1) Ti, (2) Ti-Nd, (3) Ti-Nd-PDA, (4) Ti-Nd-PDA + NIR, (5) Ti-Nd-PDA-Fc, and (6) Ti-Nd-PDA-Fc + NIR. Each group consists of three rats. Two wounds with 1−2 cm in length were made on the back of each rat. The samples were applied with MRSA bacteria (1×10^7 CFU/mL, 10 μL) and then dried in the air for 10 min for bacteria adhesion. Afterward, each sample was embedded subcutaneously into a random wound site. The wound sites were subsequently sutured after the implantations. The rats were euthanized with an inhalant anesthetic after 3 days of embedding.

https://dx.doi.org/10.1021/acsami.9b22339
ACS Appl. Mater. Interfaces 2020, 12, 8915−8928

All the wounds and contaminated tissues were photographed. Also, each substrate was removed, and the bacteria on the samples were quantified by diluted plate assay. All animal experiments adhered to the NIH Guidelines for Care and Use of Laboratory Animals (NIH publication no. 85-23 Rev. 1985) and were approved by the Research Center for Laboratory Animals of Shanghai University of Traditional Chinese Medicine.

4.10. Histology. For histology analysis, the wounds of rat were excised on the determined time and fixed in 10% formaldehyde, then embedded in paraffin, cut into sections, and finally stained with H&E dye.

4.11. Statistical Analysis. All data were expressed as means and standard deviation (SD) and analyzed using one-way ANOVA with post hoc tests. Significance was set at $p < 0.05$ (***$p < 0.001$, **$p < 0.01$, and *$p < 0.05$), while $p > 0.05$ was considered to be statistically nonsignificant (N.S.).

■ ASSOCIATED CONTENT

Supporting Information

The Supporting Information is available free of charge at https://pubs.acs.org/doi/10.1021/acsami.9b22339.

XRD spectra, TEM images, FTIR spectra, water contact angle test, heating and cooling curve of Ti-Nd-PDA-Fc, anti-adhesion test, and digital photos of NIR irradiation on the wound sites (PDF)

■ AUTHOR INFORMATION

Corresponding Authors

Xue Qu − *Key Laboratory for Ultrafine Materials of Ministry of Education, Engineering Research Centre for Biomedical Materials of Ministry of Education, School of Material Science and Engineering, East China University of Science and Technology, Shanghai 200237, China;* orcid.org/0000-0002-3410-5789; Email: quxue@ecust.edu.cn

Changsheng Liu − *Key Laboratory for Ultrafine Materials of Ministry of Education, Engineering Research Centre for Biomedical Materials of Ministry of Education, School of Material Science and Engineering, East China University of Science and Technology, Shanghai 200237, China;* Email: liucs@ecust.edu.cn

Authors

Jialin Song − *Key Laboratory for Ultrafine Materials of Ministry of Education, Engineering Research Centre for Biomedical Materials of Ministry of Education, School of Material Science and Engineering, East China University of Science and Technology, Shanghai 200237, China*

Huan Liu − *Key Laboratory for Ultrafine Materials of Ministry of Education, Engineering Research Centre for Biomedical Materials of Ministry of Education, School of Material Science and Engineering, East China University of Science and Technology, Shanghai 200237, China*

Miao Lei − *Key Laboratory for Ultrafine Materials of Ministry of Education, Engineering Research Centre for Biomedical Materials of Ministry of Education, School of Material Science and Engineering, East China University of Science and Technology, Shanghai 200237, China*

Haoqi Tan − *Key Laboratory for Ultrafine Materials of Ministry of Education, Engineering Research Centre for Biomedical Materials of Ministry of Education, School of Material Science and Engineering, East China University of Science and Technology, Shanghai 200237, China*

Zhanyi Chen − *Key Laboratory for Ultrafine Materials of Ministry of Education, Engineering Research Centre for Biomedical Materials of Ministry of Education, School of Material Science and Engineering, East China University of Science and Technology, Shanghai 200237, China*

Artem Antoshin − *Institute for Regenerative Medicine, Sechenov University, Moscow 119991, Russia*

Gregory F. Payne − *Department of Bioengineering, Institute for Biosystems and Biotechnology Research and Fischell, College Park, Maryland 20742, United States;* orcid.org/0000-0001-6638-9459

Complete contact information is available at: https://pubs.acs.org/10.1021/acsami.9b22339

Author Contributions

‖J.S. and H.L. contributed equally to this work.

Author Contributions

J.S. and H.L. designed the experiments, analyzed the data, and prepared the manuscript. M.L. and H.T. contributed to the characterization analysis. Z.C. and A.A. contributed to the cell and animal experiments. G.F.P., X.Q., and C.L. contributed to the preparation and discussion of the manuscript. All authors commented on the manuscript.

Notes

The authors declare no competing financial interest.

■ ACKNOWLEDGMENTS

The support from the National Natural Science Foundation of China (51621002, 31922041, 11932012, and 51573047), 111 Project (B14018), the Science and Technology Innovation Project of Shanghai Science and Technology Committee (18441908300), and the United States National Science Foundation (DMREF-1435957; ECCS-1807604) is acknowledged.

■ REFERENCES

(1) Hall-Stoodley, L.; Costerton, J. W.; Stoodley, P. Bacterial Biofilms: From the Natural Environment to Infectious Diseases. *Nat. Rev. Microbiol.* **2004**, *2*, 95−108.

(2) Arciola, C. R.; Campoccia, D.; Montanaro, L. Implant Infections: Adhesion, Biofilm Formation and Immune Evasion. *Nat. Rev. Microbiol.* **2018**, *16*, 397−409.

(3) Schierholz, J. M.; Beuth, J. Implant Infections: A Haven for Opportunistic Bacteria. *J. Hosp. Infect.* **2001**, *49*, 87−93.

(4) Zhang, H.; Wang, D.; Zuo, X.; Gao, C. UV-Responsive Multilayers with Multiple Functions for Biofilm Destruction and Tissue Regeneration. *ACS Appl. Mater. Interfaces* **2019**, *11*, 17283−17293.

(5) Wei, T.; Yu, Q.; Chen, H. Responsive and Synergistic Antibacterial Coatings: Fighting against Bacteria in a Smart and Effective Way. *Adv. Healthcare Mater.* **2019**, *8*, 1801381.

(6) Su, Y.; Zhi, Z.; Gao, Q.; Xie, M.; Yu, M.; Lei, B.; Li, P.; Ma, P. X. Autoclaving-Derived Surface Coating with in Vitro and in Vivo Antimicrobial and Antibiofilm Efficacies. *Adv. Healthcare Mater.* **2017**, *6*, 1601173.

(7) Coad, B. R.; Kidd, S. E.; Ellis, D. H.; Griesser, H. J. Biomaterials Surfaces Capable of Resisting Fungal Attachment and Biofilm Formation. *Biotechnol. Adv.* **2014**, *32*, 296−307.

(8) Gu, J.; Su, Y.; Liu, P.; Li, P.; Yang, P. An Environmentally Benign Antimicrobial Coating Based on a Protein Supramolecular Assembly. *ACS Appl. Mater. Interfaces* **2017**, *9*, 198−210.

(9) Ding, X.; Duan, S.; Ding, X.; Liu, R.; Xu, F. J. Versatile Antibacterial Materials: An Emerging Arsenal for Combatting Bacterial Pathogens. *Adv. Funct. Mater.* **2018**, *28*, 1802140.

(10) Yang, C.; Ding, X.; Ono, R. J.; Lee, H.; Hsu, L. Y.; Tong, Y. W.; Hedrick, J.; Yang, Y. Y. Brush-Like Polycarbonates Containing Dopamine, Cations, and PEG Providing a Broad-Spectrum,

Antibacterial, and Antifouling Surface Via One-Step Coating. *Adv. Mater.* **2014**, *26*, 7346−7351.
(11) Ding, X.; Yang, C.; Lim, T. P.; Hsu, L. Y.; Engler, A. C.; Hedrick, J. L.; Yang, Y. Y. Antibacterial and Antifouling Catheter Coatings Using Surface Grafted PEG-B-Cationic Polycarbonate Diblock Copolymers. *Biomaterials* **2012**, *33*, 6593−6603.
(12) Kwon, H. J.; Lee, Y.; Phuong, L. T.; Seon, G. M.; Kim, E.; Park, J. C.; Yoon, H.; Park, K. D. Zwitterionic Sulfobetaine Polymer-Immobilized Surface by Simple Tyrosinase-Mediated Grafting for Enhanced Antifouling Property. *Acta Biomater.* **2017**, *61*, 169−179.
(13) Hu, J.; Zheng, Z.; Liu, C.; Hu, Q.; Cai, X.; Xiao, J.; Cheng, Y. A pH-Responsive Hydrogel with Potent Antibacterial Activity against Both Aerobic and Anaerobic Pathogens. *Biomater. Sci.* **2019**, *7*, 581−584.
(14) Fathi, M.; Akbari, B.; Taheriazam, A. Antibiotics Drug Release Controlling and Osteoblast Adhesion from Titania Nanotubes Arrays Using Silk Fibroin Coating. *Mater. Sci. Eng., C* **2019**, *103*, 109743.
(15) Qi, F.; Qian, Y.; Shao, N.; Zhou, R.; Zhang, S.; Lu, Z.; Zhou, M.; Xie, J.; Wei, T.; Yu, Q.; Liu, R. Practical Preparation of Infection-Resistant Biomedical Surfaces from Antimicrobial β-Peptide Polymers. *ACS Appl. Mater. Interfaces* **2019**, *11*, 18907−18913.
(16) Thallinger, B.; Prasetyo, E. N.; Nyanhongo, G. S.; Guebitz, G. M. Antimicrobial Enzymes: An Emerging Strategy to Fight Microbes and Microbial Biofilms. *Biotechnol. J.* **2013**, *8*, 97−109.
(17) Zhao, J.; Millians, W.; Tang, S.; Wu, T.; Zhu, L.; Ming, W. Self-Stratified Antimicrobial Acrylic Coatings Via One-Step UV Curing. *ACS Appl. Mater. Interfaces* **2015**, *7*, 18467−18472.
(18) Yang, J.; Gao, G.; Zhang, X.; Ma, Y.-H.; Chen, X.; Wu, F.-G. One-Step Synthesis of Carbon Dots with Bacterial Contact-Enhanced Fluorescence Emission: Fast Gram-Type Identification and Selective Gram-Positive Bacterial Inactivation. *Carbon* **2019**, *146*, 827−839.
(19) Zhang, X.; Chen, X.; Yang, J.; Jia, H. R.; Li, Y. H.; Chen, Z.; Wu, F. G. Quaternized Silicon Nanoparticles with Polarity-Sensitive Fluorescence for Selectively Imaging and Killing Gram-Positive Bacteria. *Adv. Funct. Mater.* **2016**, *26*, 5958−5970.
(20) Xi, J.; Wei, G.; An, L.; Xu, Z.; Xu, Z.; Fan, L.; Gao, L. Copper/Carbon Hybrid Nanozyme: Tuning Catalytic Activity by the Copper State for Antibacterial Therapy. *Nano Lett.* **2019**, *19*, 7645−7654.
(21) Gatadi, S.; Madhavi, Y. V.; Chopra, S.; Nanduri, S. Promising Antibacterial Agents against Multidrug Resistant Staphylococcus Aureus. *Bioorg. Chem.* **2019**, *92*, 103252.
(22) Sies, H. Hydrogen Peroxide as a Central Redox Signaling Molecule in Physiological Oxidative Stress: Oxidative Eustress. *Redox Biol.* **2017**, *11*, 613−619.
(23) Wang, Y.; Wan, J.; Miron, R. J.; Zhao, Y.; Zhang, Y. Antibacterial Properties and Mechanisms of Gold-Silver Nanocages. *Nanoscale* **2016**, *8*, 11143−11152.
(24) Xie, X.; Mao, C.; Liu, X.; Tan, L.; Cui, Z.; Yang, X.; Zhu, S.; Li, Z.; Yuan, X.; Zheng, Y.; Yeung, K. W. K.; Chu, P. K.; Wu, S. Tuning the Bandgap of Photo-Sensitive Polydopamine/Ag3PO4/Graphene Oxide Coating for Rapid, Noninvasive Disinfection of Implants. *ACS Cent. Sci.* **2018**, *4*, 724−738.
(25) Dryden, M. Reactive Oxygen Therapy: A Novel Therapy in Soft Tissue Infection. *Curr. Opin. Infect. Dis.* **2017**, *30*, 143−149.
(26) Liu, X.; Yan, Z.; Zhang, Y.; Liu, Z.; Sun, Y.; Ren, J.; Qu, X. Two-Dimensional Metal-Organic Framework/Enzyme Hybrid Nanocatalyst as a Benign and Self-Activated Cascade Reagent for in Vivo Wound Healing. *ACS Nano* **2019**, *13*, 5222−5230.
(27) Sun, H.; Gao, N.; Dong, K.; Ren, J.; Qu, X. Graphene Quantum Dots-Band-Aids Used for Wound Disinfection. *ACS Nano* **2014**, *8*, 6202−6210.
(28) Mao, C.; Xiang, Y.; Liu, X.; Zheng, Y.; Yeung, K. W. K.; Cui, Z.; Yang, X.; Li, Z.; Liang, Y.; Zhu, S.; Wu, S. Local Photothermal/Photodynamic Synergistic Therapy by Disrupting Bacterial Membrane to Accelerate Reactive Oxygen Species Permeation and Protein Leakage. *ACS Appl. Mater. Interfaces* **2019**, *11*, 17902−17914.
(29) Jia, R.; Tian, W.; Bai, H.; Zhang, J.; Wang, S.; Zhang, J. Sunlight-Driven Wearable and Robust Antibacterial Coatings with Water-Soluble Cellulose-Based Photosensitizers. *Adv. Healthcare Mater.* **2019**, *8*, 1801591.
(30) Tong, W.; Xiong, Y.; Duan, S.; Ding, X.; Xu, F.-J. Phthalocyanine Functionalized Poly (Glycidyl Methacrylate) Nano-Assemblies for Photodynamic Inactivation of Bacteria. *Biomater. Sci.* **2019**, *7*, 1905−1918.
(31) Tang, Z.; Liu, Y.; He, M.; Bu, W. Chemodynamic Therapy: Tumour Microenvironment-Mediated Fenton and Fenton-Like Reactions. *Angew. Chem., Int. Ed.* **2019**, *58*, 946−956.
(32) Yuan, Z.; Tao, B.; He, Y.; Liu, J.; Lin, C.; Shen, X.; Yu, Y.; Mu, C.; Liu, P.; Cai, K. Biocompatible MoS2/PDA-RGD Coating on Titanium Implant with Antibacterial Property Via Intrinsic ROS-Independent Oxidative Stress and Nir Irradiation. *Biomaterials* **2019**, *217*, 119290.
(33) Guan, M.; Chen, Y.; Wei, Y.; Song, H.; Gao, C.; Cheng, H.; Li, Y.; Huo, K.; Fu, J.; Xiong, W. Long-Lasting Bactericidal Activity through Selective Physical Puncture and Controlled Ions Release of Polydopamine and Silver Nanoparticles-Loaded TiO_2 Nanorods in Vitro and in Vivo. *International Journal of Nanomedicine* **2019**, *14*, 2903−2914.
(34) Wang, Y.; Huang, Q.; He, X.; Chen, H.; Zou, Y.; Li, Y.; Lin, K.; Cai, X.; Xiao, J.; Zhang, Q.; Cheng, Y. Multifunctional Melanin-Like Nanoparticles for Bone-Targeted Chemo-Photothermal Therapy of Malignant Bone Tumors and Osteolysis. *Biomaterials* **2018**, *183*, 10−19.
(35) Liu, M.; Zeng, G.; Wang, K.; Wan, Q.; Tao, L.; Zhang, X.; Wei, Y. Recent Developments in Polydopamine: An Emerging Soft Matter for Surface Modification and Biomedical Applications. *Nanoscale* **2016**, *8*, 16819−16840.
(36) Sadrearhami, Z.; Shafiee, F. N.; Ho, K. K. K.; Kumar, N.; Krasowska, M.; Blencowe, A.; Wong, E. H. H.; Boyer, C. Antibiofilm Nitric Oxide-Releasing Polydopamine Coatings. *ACS Appl. Mater. Interfaces* **2019**, *11*, 7320−7329.
(37) Gao, G.; Jiang, Y.-W.; Jia, H.-R.; Wu, F.-G. Near-Infrared Light-Controllable On-Demand Antibiotics Release Using Thermo-Sensitive Hydrogel-Based Drug Reservoir for Combating Bacterial Infection. *Biomaterials* **2019**, *188*, 83−95.
(38) Gao, Q.; Feng, T.; Huang, D.; Liu, P.; Lin, P.; Wu, Y.; Ye, Z.; Ji, J.; Li, P.; Huang, W. Antibacterial and Hydroxyapatite-Forming Coating for Biomedical Implants Based on Polypeptide-Functionalized Titania Nanospikes. *Biomater. Sci.* **2020**, *8*, 278−289.
(39) Li, M.; Liu, X.; Xu, Z.; Yeung, K. W. K.; Wu, S. Dopamine Modified Organic-Inorganic Hybrid Coating for Antimicrobial and Osteogenesis. *ACS Appl. Mater. Interfaces* **2016**, *8*, 33972−33981.
(40) Liu, H.; Qu, X.; Tan, H.; Song, J.; Lei, M.; Kim, E.; Payne, G. F.; Liu, C. Role of Polydopamine's Redox-Activity on Its Pro-Oxidant, Radical-Scavenging, and Antimicrobial Activities. *Acta Biomater.* **2019**, *88*, 181−196.
(41) Forooshani, P. K.; Polega, E.; Thomson, K.; Bhuiyan, M. S. A.; Pinnaratip, R.; Trought, M.; Kendrick, C.; Gao, Y.; Perrine, K. A.; Pan, L.; Lee, B. P. Antibacterial Properties of Mussel-Inspired Polydopamine Coatings Prepared by a Simple Two-Step Shaking-Assisted Method. *Front. Chem.* **2019**, *7*, 631.
(42) Meng, H.; Forooshani, P. K.; Joshi, P. U.; Osborne, J.; Mi, X.; Meingast, C.; Pinnaratip, R.; Kelley, J.; Narkar, A.; He, W.; Frost, M. C.; Heldt, C. L.; Lee, B. P. Biomimetic Recyclable Microgels for On-Demand Generation of Hydrogen Peroxide and Antipathogenic Application. *Acta Biomater.* **2019**, *83*, 109−118.
(43) Kwon, B.; Han, E.; Yang, W.; Cho, W.; Yoo, W.; Hwang, J.; Kwon, B.-M.; Lee, D. Nano-Fenton Reactors as a New Class of Oxidative Stress Amplifying Anticancer Therapeutic Agents. *ACS Appl. Mater. Interfaces* **2016**, *8*, 5887−5897.
(44) Zhuk, I.; Jariwala, F.; Attygalle, A. B.; Wu, Y.; Libera, M. R.; Sukhishvili, S. A. Self-Defensive Layer-by-Layer Films with Bacteria-Triggered Antibiotic Release. *ACS Nano* **2014**, *8*, 7733−7745.
(45) Lu, Y.; Wu, Y.; Liang, J.; Libera, M. R.; Sukhishvili, S. A. Self-Defensive Antibacterial Layer-by-Layer Hydrogel Coatings with pH-Triggered Hydrophobicity. *Biomaterials* **2015**, *45*, 64−71.

https://dx.doi.org/10.1021/acsami.9b22339
ACS Appl. Mater. Interfaces 2020, 12, 8915−8928

(46) Branitzki-Heinemann, K.; Brogden, G.; von Köckritz-Blickwede, M. Influence of Oxygen on Function and Cholesterol Composition of Murine Bone Marrow-Derived Neutrophils. In *Neutrophil*, Springer: 2020; pp 223−233.
(47) Kempf, V. A. J.; Lebiedziejewski, M.; Alitalo, K.; Wälzlein, J.-H.; Ehehalt, U.; Fiebig, J.; Huber, S.; Schütt, B.; Sander, C. A.; Müller, S.; Grassl, G.; Yazdi, A. S.; Brehm, B.; Autenrieth, I. B. Activation of Hypoxia-Inducible Factor-1 in Bacillary Angiomatosis: Evidence for a Role of Hypoxia-Inducible Factor-1 in Bacterial Infections. *Circulation* **2005**, *111*, 1054−1062.
(48) Tang, Z.; Zhang, H.; Liu, Y.; Ni, D.; Zhang, H.; Zhang, J.; Yao, Z.; He, M.; Shi, J.; Bu, W. Antiferromagnetic Pyrite as the Tumor Microenvironment-Mediated Nanoplatform for Self-Enhanced Tumor Imaging and Therapy. *Adv. Mater.* **2017**, *29*, 1701683.
(49) Liu, B.; Aydil, E. S. Growth of Oriented Single-Crystalline Rutile TiO_2 Nanorods on Transparent Conducting Substrates for Dye-Sensitized Solar Cells. *J. Am. Chem. Soc.* **2009**, *131*, 3985−3990.
(50) Kumar, T. N.; Sivabalan, S.; Chandrasekaran, N.; Phani, K. L. N. Ferrocene-Functionalized Polydopamine as a Novel Redox Matrix for H_2O_2 Oxidation. *J. Mater. Chem. B* **2014**, *2*, 6081−6088.
(51) Dong, L.; Cheng, K.; Weng, W.; Song, C.; Du, P.; Shen, G.; Han, G. Hydrothermal Growth of Rutile TiO2 Nanorod Films on Titanium Substrates. *Thin Solid Films* **2011**, *519*, 4634−4640.
(52) Gao, Q.; Li, P.; Zhao, H.; Chen, Y.; Jiang, L.; Ma, P. X. Methacrylate-Ended Polypeptides and Polypeptoids for Antimicrobial and Antifouling Coatings. *Polym. Chem.* **2017**, *8*, 6386−6397.
(53) Kim, Y. W.; Modigunta, J. K. R.; Male, U.; Huh, D. S. Effect of Ferrocene on the Fabrication of Honeycomb-Patterned Porous Polystyrene Films and Silver Functionalization of the Film. *Polymer* **2019**, *166*, 55−62.
(54) Srisuk, P.; Correlo, V. M.; Leonor, I. B.; Palladino, P.; Reis, R. L. Redox Activity of Melanin from the Ink Sac of Sepia Officinalis by Means of Colorimetric Oxidative Assay. *Nat. Prod. Res.* **2016**, *30*, 982−986.
(55) Wang, H.; Li, P.; Yu, D.; Zhang, Y.; Wang, Z.; Liu, C.; Qiu, H.; Liu, Z.; Ren, J.; Qu, X. Unraveling the Enzymatic Activity of Oxygenated Carbon Nanotubes and Their Application in the Treatment of Bacterial Infections. *Nano Lett.* **2018**, *18*, 3344−3351.
(56) Wang, Q.; Tian, S.; Ning, P. Degradation Mechanism of Methylene Blue in a Heterogeneous Fenton-Like Reaction Catalyzed by Ferrocene. *Ind. Eng. Chem. Res.* **2014**, *53*, 643−649.
(57) Jansson, T.; Clare-Salzler, Z. J.; Zaveri, T. D.; Mehta, S.; Dolgova, N. V.; Chu, B. H.; Ren, F.; Keselowsky, B. G. Antibacterial Effects of Zinc Oxide Nanorod Surfaces. *J. Nanosci. Nanotechnol.* **2012**, *12*, 7132−7138.
(58) Wang, B.-l.; Ren, K.-f.; Chang, H.; Wang, J.-l.; Ji, J. Construction of Degradable Multilayer Films for Enhanced Antibacterial Properties. *ACS Appl. Mater. Interfaces* **2013**, *5*, 4136−4143.
(59) Li, M.; Li, L.; Su, K.; Liu, X.; Zhang, T.; Liang, Y.; Jing, D.; Yang, X.; Zheng, D.; Cui, Z.; Li, Z.; Zhu, S.; Yeung, K. W. K.; Zheng, Y.; Wang, X.; Wu, S. Highly Effective and Noninvasive Near-Infrared Eradication of a Staphylococcus Aureus Biofilm on Implants by a Photoresponsive Coating within 20 Min. *Adv. Sci.* **2019**, *6*, 1900599.
(60) Lei, M.; Qu, X.; Liu, H.; Liu, Y.; Wang, S.; Wu, S.; Bentley, W. E.; Payne, G. F.; Liu, C. Programmable Electrofabrication of Porous Janus Films with Tunable Janus Balance for Anisotropic Cell Guidance and Tissue Regeneration. *Adv. Funct. Mater.* **2019**, *29*, 1900065.

https://dx.doi.org/10.1021/acsami.9b22339
ACS Appl. Mater. Interfaces 2020, 12, 8915−8928